

Noninvasive Diagnosis of High-Grade Urothelial Carcinoma in Urine by Raman Spectral Imaging

Hesham K. Yosef,[†] Sascha D. Krauß,[†] Tatjana Lechtonen,[†] Hendrik Jütte,[‡] Andrea Tannapfel,[‡] Heiko U. Käfferlein,[§] Thomas Brüning,[§] Florian Roghmann,^{||} Joachim Noldus,^{||} Axel Mosig,[†] Samir F. El-Mashtoly,[†] and Klaus Gerwert^{*,†}

[†]Department of Biophysics, Ruhr-University Bochum, 44780 Bochum, Germany

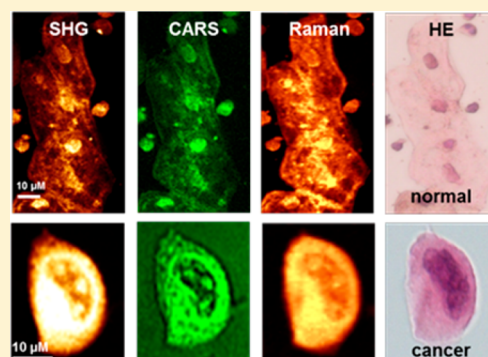
[‡]Bergmannsheil Hospital, Ruhr-University Bochum, 44789 Bochum, Germany

[§]Institute for Prevention and Occupational Medicine of the German Social Accident Insurance, Institute of the Ruhr-University Bochum (IPA), 44789 Bochum, Germany

^{||}Department of Urology, Marien Hospital Herne, Ruhr-University Bochum, 44625 Herne, Germany

Supporting Information

ABSTRACT: The current gold standard for the diagnosis of bladder cancer is cystoscopy, which is invasive and painful for patients. Therefore, noninvasive urine cytology is usually used in the clinic as an adjunct to cystoscopy; however, it suffers from low sensitivity. Here, a novel noninvasive, label-free approach with high sensitivity for use with urine is presented. Coherent anti-Stokes Raman scattering imaging of urine sediments was used in the first step for fast preselection of urothelial cells, where high-grade urothelial cancer cells are characterized by a large nucleus-to-cytoplasm ratio. In the second step, Raman spectral imaging of urothelial cells was performed. A supervised classifier was implemented to automatically differentiate normal and cancerous urothelial cells with 100% accuracy. In addition, the Raman spectra not only indicated the morphological changes that are identified by cytology with hematoxylin and eosin staining but also provided molecular resolution through the use of specific marker bands. The respective Raman marker bands directly show a decrease in the level of glycogen and an increase in the levels of fatty acids in cancer cells as compared to controls. These results pave the way for “spectral” cytology of urine using Raman microspectroscopy.



Bladder cancer is the ninth most common cancer in the world, with around 429 000 new cases diagnosed and 150 000 deaths every year.^{1,2} The majority of bladder tumors are urothelial carcinoma (UC). Usually, bladder cancer is detected at an early stage (nonmuscle invasive, low grade) when it can be treated easily.³ The current gold standard for bladder cancer detection is cystoscopy, which is invasive and uncomfortable for patients and has a utility that depends on the experience and ability of the examiner.³ As bladder cancer is likely to recur, patients with a history of UC often undergo follow-up tests to monitor for recurrence for years after therapy. As a result, bladder cancer is one of the most costly of cancer diseases.⁴

Noninvasive diagnosis of UC remains challenging. The only noninvasive diagnostic method used in clinical practice is urine cytology, which is used as an adjunct to cystoscopy. The specificity of cytology is higher than 90% and the sensitivity is ~80% for high-grade UC, whereas the sensitivity is very low (~20–53%) in the case of low-grade UC.^{5,6} Several urine-based tests have been developed over the last 2 decades, but none of them is recommended in the European Association of Urology guidelines for the diagnosis and treatment of bladder cancer.³

Raman microspectroscopy is a powerful method that has been applied for the analysis of biological and biomedical samples.^{7–13} For instance, invasive diagnosis of bladder cancer has been reported using Raman spectroscopy.^{14–22} Recent studies have also shown the potential of Raman microspectroscopy to analyze and discriminate between normal and cancer cells using bladder cell lines.^{14,23–25} Shapiro et al. were the first group to apply Raman microspectroscopy to urine. They demonstrated the feasibility of this method for the analysis of urine even though the results and conclusions of their study remain debatable.²⁶ Their results demonstrated the presence of a Raman peak near 1584 cm⁻¹ only in high- and low-grade tumors but not in normal urothelial cells. On the basis of these findings, the authors found a high accuracy association of this Raman peak and postulated that it is characteristic for urothelial cancer cells.²⁶

Here, we report a combination of Raman, coherent anti-Stokes Raman scattering (CARS), and second harmonic

Received: April 14, 2017

Accepted: May 25, 2017

Published: May 25, 2017

generation (SHG) images of urine from patients with pathologically confirmed high-grade UC and those without UC. We found that the Raman band near 1584 cm^{-1} originated from erythrocytes, suggesting that the previously reported Raman spectra²⁶ of UC in urine cells originate mostly from blood cells, especially in the case of high-grade urothelial cancer cells. With these results, Raman and CARS/SHG imaging of normal and cancerous urothelial cells free from erythrocyte contamination was performed to monitor the changes in the biochemical status of urothelial cells as a result of cancer progression. Furthermore, a supervised learning algorithm based on random forest as a classifier was trained and used to differentiate normal and cancer urothelial cells with 100% accuracy using leave-one-patient-out cross-validation.

EXPERIMENTAL SECTION

Urine Sampling. Urine samples were collected (prior TUR-B) from 10 patients diagnosed with high-grade UC and from 10 patients with pathologically confirmed urocystitis but without UC at the Department of Urology of the Ruhr-University Bochum, Marien Hospital Herne, Germany. Institutional review board approval (IRB 3674-10) and written informed consent from all patients were obtained. Urine samples were collected directly from patients. The preparation of urine samples for spectroscopic measurements is described in the Supporting Information and shown in Figure S1.

CARS and SHG Microscopic Imaging. CARS images were acquired using a commercial setup (TCS SP5 II CARS; Leica Microsystems, Heidelberg, Germany) consisting of a picosecond pulsed laser (APE picoEmerald, Berlin, Germany) that can generate and synchronize two collinearly aligned beams to a confocal inverted microscope, as described in detail previously.²⁷ The pump and Stokes wavelengths were 810.5 and 1064 nm, respectively. Laser beams are focused in the microscope using an HCX IRAPO L (25 \times /0.95W, Leica Microsystems) water immersion objective. CARS and SHG images were collected simultaneously at 2935 cm^{-1} with a pixel dwell time of 180 μs and resolution of 500 nm.

Raman Spectral Imaging. Raman measurements of urine cells were acquired using an alpha300 RA confocal Raman microscope (WITec, Ulm, Germany) as indicated previously.^{28–30} The Raman excitation source is a frequency-doubled Nd:YAG laser 532 nm (CrystaLaser, Reno, NV, USA). The laser beam is coupled to a Zeiss microscope using a wavelength-specific single-mode optical fiber. The laser beam is collimated and then focused on the sample through a Nikon NIR APO (60 \times /1.00 NA) water immersion objective. The sample was fixed on a piezoelectrically driven microscope scanning stage. The backscattered Raman light was collected and finally detected by a back-illuminated deep-depletion charge-coupled device camera, which can detect the Raman signal. Raman spectral imaging was conducted utilizing a raster scanning laser beam over cells to acquire full Raman spectra at a speed of 0.5 s per pixel, with a pixel resolution of 500 nm.

Data Processing and Multivariate Analysis. To collect the training data, hierarchical cluster analysis (HCA) was first performed on the Raman spectral data from cells. Raman hyperspectral results were exported to Matlab (The MathWorks, Natick, MA, USA). In-house built scripts were implemented for data preprocessing and HCA. All Raman spectra without a C–H band at $2850\text{--}3000\text{ cm}^{-1}$ were treated as background and deleted. To remove cosmic spikes, an impulse noise filter was applied and the Raman spectra were

interpolated to a reference wavenumber scale. All Raman spectra were baseline-corrected with a third-order polynomial. Furthermore, all spectra were vector normalized. HCA was performed on the regions of $400\text{--}1800$ and $2800\text{--}3050\text{ cm}^{-1}$ using Ward's clustering combined with Pearson's correlation distance. The resolution of hematoxylin and eosin (HE) images was reduced from 0.14 to 0.5 $\mu\text{m}/\text{pixel}$ to match the resolution of the corresponding Raman images and converted to grayscale. A suitable intensity threshold value was determined to generate a two-color-channel image. In this two-color-channel image, a certain color intensity threshold was set to separate the nucleus from the cell based on HE staining. Values above this threshold were considered to be the nucleus and denoted in blue. The remaining cellular parts (cytoplasm) are denoted in red. This image was then automatically registered with the HCA of the Raman image. Colocalization between the two-color-channel image and the HCA image was applied to determine the "best matching clusters" for the nucleus and cytoplasm as illustrated previously.^{27,31} This algorithm was applied on 61 normal cells and 60 high-grade cancer urothelial cells and produced 161 937 and 375 203 Raman spectra from normal and high-grade cancer urothelial cells, respectively. These spectra were used to train a random forest classifier. Afterward, several random forest data sets were trained and subsequently validated. The validation was performed by means of leave-one-patient-out cross-validation. This was achieved by leaving out every patient once, training on the others, and validating with the one that was left out. This procedure was repeated for every patient, and the results were averaged, which means that every patient is in the validation cohort once and in the training cohort $N - 1$ times but never in both at the same time.³¹

RESULTS AND DISCUSSION

Identification of Urothelial Cells in Urine Sediments.

Raman spectra of different cells in urine sediments, such as normal and high-grade cancerous urothelial cells, squamous cells, leukocytes, erythrocytes, and bacteria, were acquired, and the results are displayed in Figure 1. Raman spectral imaging is capable of differentiating these cells. For instance, a normal

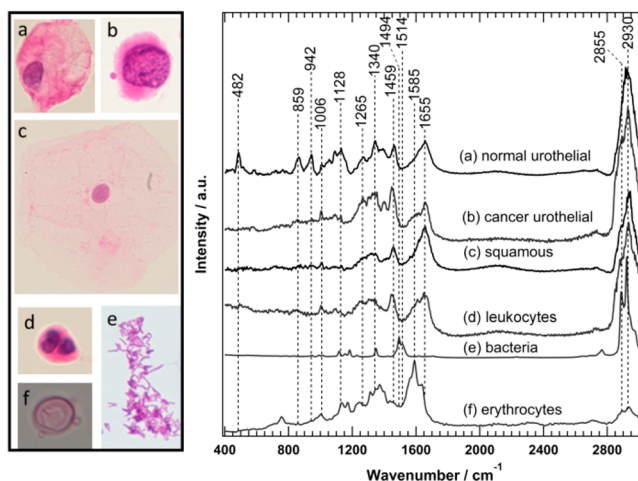


Figure 1. Raman spectra and HE-stained images of different cells in urine such as (a) normal and (b) cancerous urothelial cells, (c) a squamous cell, (d) a leukocyte, (e) bacteria, and (f) an erythrocyte. This urine sample was not filtered in order to measure Raman spectra of different cell types in urine.

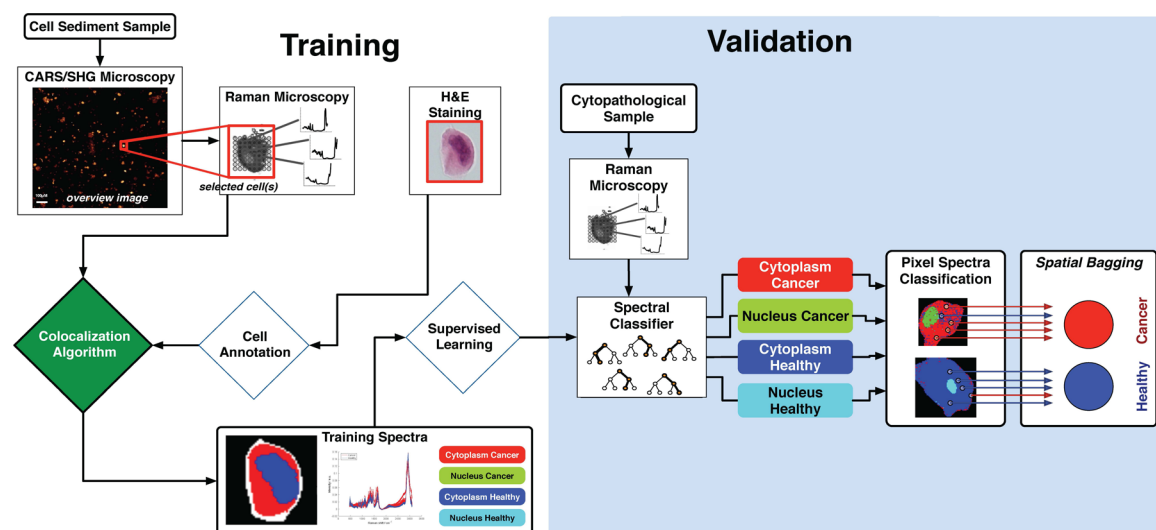


Figure 2. Workflow for the training and validation stages of the random forest classifier.

urothelial cell (a) is characterized by a Raman band near 482 cm^{-1} , which is absent in the spectrum of high-grade urothelial cancer cells (b). Erythrocytes (f) have a strong heme band near 1585 cm^{-1} , which is also absent in the spectrum of leukocytes (d). Bacteria (e) can be distinguished from other cells by their Raman doublet near $1494/1514\text{ cm}^{-1}$ and sharp bands near 2285 and 2922 cm^{-1} . These spectral differences can be used to differentiate cell types and identify urothelial cancer cells in urine. However, it is not feasible to acquire Raman measurements for all of these cells in each patient's sample. This is because Raman scattering is weak, which makes the time of data acquisition long and thus the entire measurement will be time-consuming. Therefore, we established the following workflow to identify urothelial cells in urine.

Workflow for the Identification of Urothelial Cells in Urine. Basically, the workflow involves a training stage followed by a validation stage (Figure 2). The aim of the training step was to first identify urothelial cells in urine and to obtain representative spectra for the urothelial cellular components, which can be used to train a supervised classifier. CARS and SHG imaging techniques were used to acquire images of urine to identify urothelial cells. Subsequently, the identified cells were measured by Raman spectral imaging. The spectral image was overlaid with its HE-stained counterpart to perform colocalization analysis to obtain representative training spectra for urothelial cells and their subcellular components.

A representative example of the different imaging results from one patient's urine is presented in detail. Figure S2 displays SHG (A) and CARS (B) images of a large area of urine sediment ($1\text{ mm} \times 1\text{ mm}$) from a patient diagnosed with high-grade UC. These images were measured simultaneously within a few minutes and used for the fast screening of urothelial cells. Other approaches for fast cancer diagnosis by Raman microscopy have been reported.^{9,11,13} For instance, a combination of autofluorescence and Raman microscopy was used.^{9,13} Here, cancerous urothelial cells were identified using label-free CARS/SHG images in a similar manner as that by pathologists using HE-stained images. The high-grade urothelial cancer cells are characterized by a high nucleus-to-cytoplasm ratio and a large distortion of their nuclear morphology compared to normal cells.³² The same criteria were used to identify high-grade urothelial cancer cells using

CARS/SHG images. Urothelial cancer cells were detected in all samples measured by CARS/SHG imaging. Around 90% of these cells were confirmed by a pathologist using the HE-stained images of the same cells to be high-grade urothelial cancer cells.

In Figure 3, the magnified SHG (panels A and F) and CARS (panels B and G) images of normal and cancerous urothelial

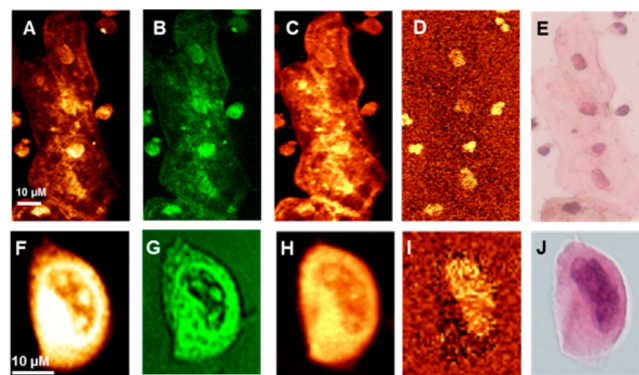


Figure 3. Different imaging techniques applied to normal (A–E) and high-grade cancerous (F–J) urothelial cells in urine sediments: (A, F) SHG images, (B, G) CARS images, (C, D, H, I) integrated Raman intensity of cells in the (C, H) $2800\text{--}3050\text{ cm}^{-1}$ and (D, I) in $785\text{--}805\text{ cm}^{-1}$ regions, and (E, J) HE-stained images.

cells are depicted. Nuclei are clearly visible in both the SHG and CARS images. Raman spectral imaging of these selected cells was performed subsequently, and integrated intensity images in the C–H stretching region of the candidate normal and high-grade cancerous urothelial cells are shown in panels C and H, respectively. The nuclei of cells can be visualized through an integration of the Raman intensity around the DNA marker band (790 cm^{-1}),³³ as displayed in panels D and I. Cells were HE-stained after the Raman measurements were completed, and a pathologist annotated the HE-stained cells shown in panels E and J as normal and high-grade cancerous urothelial cells, respectively, thus confirming our preselection.

It is obvious that the Raman images (panels D and I) can reproduce the same characterization of the cell nucleus in a label-free manner as that obtained with the HE-stained images

(panels E and J). The nuclei of cells are also visible in the SHG and CARS images. It has been reported that SHG can be used to visualize collagen and myosin structures in cells.³⁴ Myosin is present in the nucleus and is involved in many nuclear functions such as transcription processes.³⁵ This may explain why the nuclei were observed more clearly with SHG in comparison with the CARS technique, which monitors the protein distribution in cells at 2935 cm^{-1} .^{36,37} Therefore, SHG and CARS were used for a fast preselection of urothelial cells in urine based on the morphological features of the cell and the ratio of the nucleus to the cytoplasm. These results set the stage for the automatic identification of urothelial cancer cells using CARS/SHG imaging.

Colocalization. The Raman spectral images were overlaid with their HE counterparts to perform colocalization analysis, and an example of the colocalization procedure is shown in detail in Figure 4.

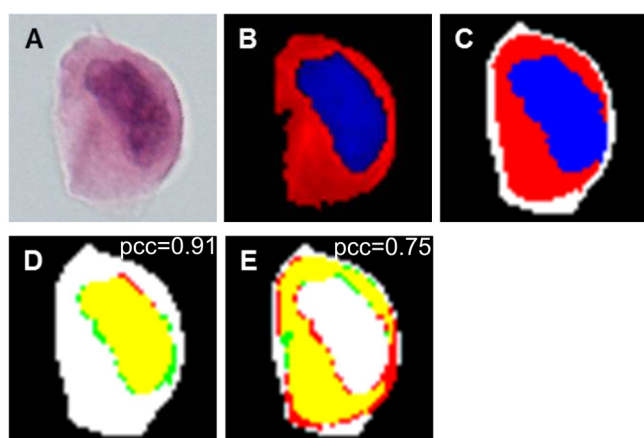


Figure 4. Colocalization of the nucleus and cytoplasm of a urothelial cell. (A) HE staining of a high-grade urothelial cancer cell. (B) Two-color-channel image of the HE-stained cell showing the nucleus (blue) and cytoplasm (red). (C) Best matching clusters from the HCA result according to the colocalization with the two color channels. Overlaid images of the nucleus and cytoplasm from the two color channels (red) in panel B with their corresponding HCA clusters (green) in panel C are displayed in panels D and E, respectively. Overlapping regions are shown in yellow.

This overlay is quantitatively determined by Pearson's correlation coefficient (PCC). Similar approaches have been used to identify subcellular organelles by Raman and CARS microscopy using fluorescence imaging as a reference.^{27,31} HE staining was performed after Raman spectral imaging measurements were recorded as depicted in Figure 4A. A two-color-channel image (panel B) was created from the HE-stained image to segment the cell into the nucleus (blue) and cytoplasm (red). Colocalization analysis transfers the nucleus and cytoplasm from the HE image into best matching clusters in the HCA of the Raman image, as displayed in panel C, where the nucleus and cytoplasm are shown in blue and red, respectively. By superimposing these clusters with their corresponding two color channels, the region of overlap is displayed in yellow. The overlapping regions agree strongly, as indicated by PCC values of 0.91 for the nucleus (panel D) and 0.75 for the cytoplasm (panel E). The spectra obtained from the colocalization algorithm are used to train a classifier. The classifier is trained independently with nucleus spectra, cytoplasm spectra, or full-cell spectra.

Raman Spectral Differences between Normal and Cancerous Urothelial Cells. The Raman mean spectra of the normal and high-grade cancerous urothelial cells used to train the classifier are shown in Figure 5. The Raman mean spectrum

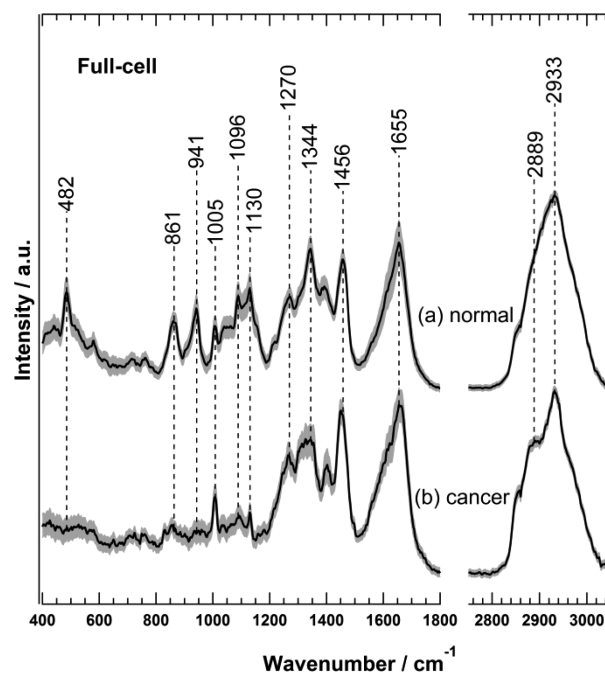


Figure 5. Raman mean spectra of (a) normal and (b) high-grade cancerous urothelial cells used for to train the random forest classifier.

of normal urothelial cells (spectrum a) displays Raman bands in the C–H stretching region at 2933 and 2889 cm^{-1} and in the fingerprint region at 1655 cm^{-1} (carbonyl stretching, amide I), 1456 cm^{-1} (CH_2 bending deformation), $1344/1270\text{ cm}^{-1}$ (amide III), 1130 cm^{-1} (C–C skeletal stretching), 1096 cm^{-1} (symmetric PO_2^- stretching), 1005 cm^{-1} (phenylalanine ring-breathing), 941 cm^{-1} (C–C stretch backbone/glycogen), 861 cm^{-1} (Tyr/glycogen), and 482 cm^{-1} (glycogen).^{15,38–40} This spectrum is also similar to the Raman spectrum of normal urothelial cells reported by Shapiro et al.²⁶ The Raman mean spectrum of the high-grade urothelial cancer cells (Figure 5b) is similar to that of normal cells (Figure 5a). However, the Raman bands at 941 , 861 , and 482 cm^{-1} have almost disappeared in the spectrum of the urothelial cancer cells. These results indicate that these three Raman bands can be used as markers to differentiate normal and high-grade cancerous urothelial cells. Similar results were obtained from the Raman mean spectra of the nucleus and cytoplasm (Figure S3) of normal and high-grade cancerous urothelial cells used for to train the classifiers.

Furthermore, the presented Raman spectrum of high-grade urothelial cancer cells (Figure 5b) is significantly different compared to that reported by Shapiro et al. characterized by a strong Raman band near 1584 cm^{-1} .²⁶ Their Raman spectrum resembles hemoglobin in erythrocytes,⁴¹ which is characterized by a strong Raman band near 1585 cm^{-1} , as shown in Figures 1F and S4. These spectra^{26,41} were acquired with 532 nm excitation, where the hemoglobin of erythrocytes is under resonance conditions.³³ This leads to obtain the resonance Raman spectra of the heme of hemoglobin being obtained, which has very strong Raman bands compared to those of other cellular or tissue components. All of these results taken together

suggest that the reported Raman spectra of UC in the urine cells of Shapiro et al. originate mostly from blood cells, especially in the case of high-grade urothelial cancer cells.²⁶ Thus, the differentiation between normal and cancerous urothelial cells was mainly based on the presence or absence of blood contamination. This means that Shapiro et al. merely described the characteristic Raman spectrum for the detection of hematuria, which is an established but not exclusive symptom of UC.³ The presence of blood in urine occurs not only due to bladder cancer but also occurs due to several other diseases such as urinary tract infection, kidney infections, or a bladder or kidney stone.^{42,43} Thus, the Raman band near 1585 cm^{-1} cannot be used as a marker for UC as it might fail to distinguish between UC and the aforementioned conditions. Therefore, the present study is the first to describe the characteristic Raman spectrum of urothelial cancer cells. To elucidate the underlying molecules within the cell using the Raman bands, Raman difference spectra (normal – cancer) between normal and cancerous urothelial cells were recorded (Figure 6b). The Raman difference spectra reveal large spectral

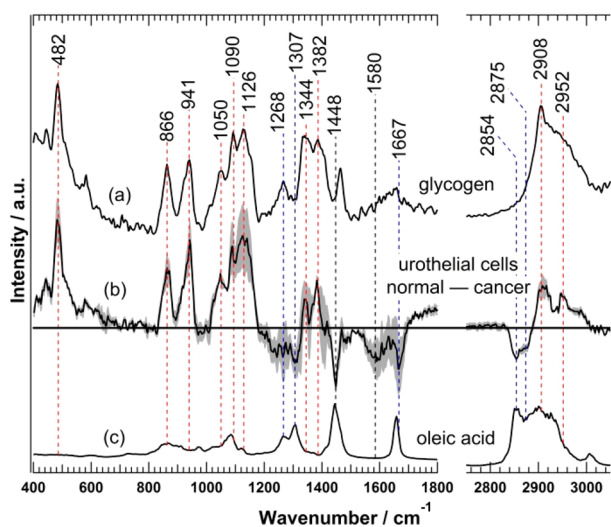


Figure 6. Comparison of the Raman difference spectrum (normal – cancer) of urothelial cells (b) with the Raman spectra of pure compounds of glycogen (a) and oleic acid (c).

changes near the 2952, 2908, 2875, 2854, 1667, 1580, 1448, 1382, 1344, 1307, 1268, 1126, 1090, 1050, 941, 866, and 482 cm^{-1} bands. Positive and negative bands in the difference spectra mean higher contributions from normal and cancer cells, respectively. Similar spectral changes were also detected in the nucleus and cytoplasm (Figure S3). These results are in agreement with the pathological grading of UC. This is because it depends on a shift in the nuclear–cytoplasmic ratio and a large distortion in the nuclear morphology, which imply that there are large changes in the nucleus and cytoplasm.³²

The difference spectrum of urothelial cells (Figure 6b) was compared to the Raman spectra of pure compounds of glycogen (a) and a fatty acid such as oleic acid (c). Interestingly, all positive and negative bands in the difference spectrum (except 1580 cm^{-1}) overlap well with bands of pure glycogen and fatty acid, respectively.

In addition, the negative band in the difference spectrum (b) at 1580 cm^{-1} could be assigned to the pyrimidine ring of nucleic acids.^{15,22} From the Raman band assignment, we can conclude that the level of glycogen is significantly decreased in

high-grade cancerous urothelial cells (Figure S5), whereas that of fatty and nucleic acids is increased compared to levels in normal urothelial cells. This is a breakthrough in Raman image analysis because the underlying metabolic changes are now directly observed in the label-free Raman spectra. Glycogen is known to be the main energy source detected in human cells. The association of glycogen metabolism with cancer development was recently indicated.^{44,45} Glycogen degradation stimulates the synthesis of fatty acids, nucleotides, nucleic acids, and aromatic amino acids.⁴⁵ These biomolecules are the building blocks for cell proliferation and cancer progression.^{44–46} Thus, it is expected that normal cells will have glycogen in abundance, whereas there will be a deficit of glycogen in cancer cells, as observed in the present study. Our findings corroborate previous studies that reported a higher level of glycogen in benign epithelial tissues, such as esophageal tissues, whereas greater concentrations of nucleic acids were found in neoplastic tissue.^{15,22}

To confirm that glycogen is localized within normal urothelial cells but not precipitated on the cell surface, we performed confocal z-stack Raman imaging of the same cells (Figure 7). Panel B(1–5) shows integrated Raman intensity

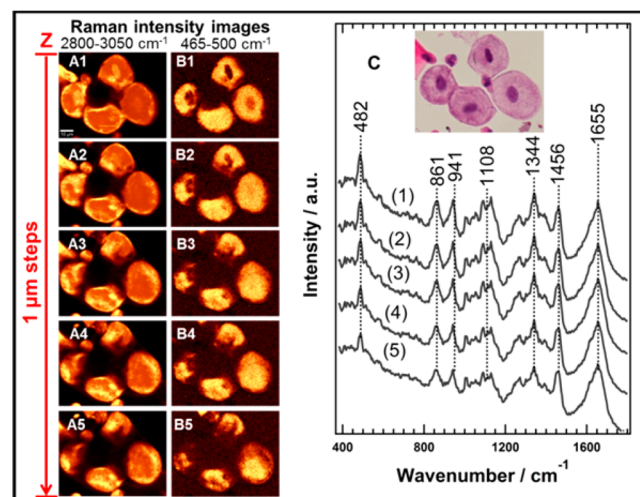


Figure 7. Confocal z-stack Raman imaging of normal urothelial cells. (A1–5, B1–5) Integrated Raman intensity images in the 2800–3050 cm^{-1} and 465–500 cm^{-1} regions of normal urothelial cells, respectively. (C) Raman mean spectra of cells measured in the z-stack. An HE-stained image is also shown.

images around the 482 cm^{-1} band of normal urothelial cells. Panel C displays the Raman spectra of cells measured in the z-stack. All of these spectra contain the 482 cm^{-1} band, which is assigned to glycogen. Thus, panel B(1–5) shows and proves the confocal distribution of glycogen within normal cells.

Validation Stage. On the basis of the classifications accomplished in the training stage, random forest classifiers were trained to perform supervised classification and to identify the nucleus and cytoplasm of both normal and high-grade cancerous urothelial cells. Random forest is an attractive classifier because it does not require feature selection before training; it is effective in both training and validation, and it is strong against overfitting.⁴⁷ We have recently used random forest to automatically identify subcellular organelles and to annotate colon tissue types and the area of colon cancer using Raman and CARS microscopy.^{27,31,41} Random forest classifiers

are validated here in a straightforward manner using leave-one-patient-out cross-validation, where all spectra employed for the training step were excluded from the validation step. The differentiation between normal and cancerous urothelial cells in urine sediments was achieved with high accuracy, as indicated in Tables 1 and S1. For instance, when calculating the number

Table 1. Classification of Urothelial Cells in Urine

classification	nucleus	cytoplasm	full-cell
sensitivity (%)	90	100	100
specificity (%)	90	100	100
accuracy (%)	90	100	100

of patients correctly classified within the left-out patients, the classifiers trained on the spectra of either full-cell or cytoplasm produced an accuracy of 100%, which is higher than that obtained when the classifier was trained with nucleus spectra (90%).

The most informative wavenumber regarding the accuracy was identified via feature selection of the random forest trained on the spectra of the full cell. During training, every wavenumber is permuted to check the change in the resulting accuracy. The higher the mean drop in accuracy, the more important the respective wavenumber is for distinguishing the different classes. The 482 cm^{-1} wavenumber was associated with the biggest drop in accuracy. These results are in agreement with the Raman difference spectrum (normal – cancer) that revealed large changes (Figure 6b) including a strong positive band at 482 cm^{-1} , which originates from glycogen. This band is present only in the spectra of normal urothelial cells and is absent in the spectra of high-grade urothelial cancer cells. It is also absent in other urine cells (Figure 1). Thus, the 482 cm^{-1} band can be used as a marker to differentiate normal and high-grade cancerous urothelial cells. Interestingly, this band was also observed in the Raman spectrum of normal bladder tissue²² and as a positive band in the Raman difference spectrum (normal – cancer) of esophagus tissues, implying the presence of a high level of glycogen in normal tissues.¹⁵

Raman spectroscopy has been used for the diagnosis of bladder cancer for more than a decade. For instance, it has been used during cystoscopy to classify bladder urothelial tissues with sensitivities and specificities of 79–89%.^{16–19} Raman spectroscopy has also been applied to differentiate different pathological grades of bladder tissue taken from patients with sensitivities and specificities of 92–98%.^{20–22} In the present study, we have established a noninvasive diagnostic tool using an easily accessible liquid biopsy taken from the patient's urine, which is in contrast to the aforementioned invasive methods based on tissue analysis.^{16–22} By using Raman microspectroscopy, cancerous urothelial cells were identified with a very high accuracy of 100%. There are several tests based on urine, such as NMP22 and FISH UroVysion, in addition to urine cytology. These tests are approved by the U.S. Food and Drug Administration.^{48–52} These tests have a low sensitivity of only 28–45%, but they have a high specificity of 97–98.5%, as shown in the prospective Uroscreen studies.^{51–53} The approach presented here seems superior to the conventionally used biomarkers.

Principally, there are two scenarios in which the results of the present study might aid clinicians in daily practice. Raman microspectroscopy could be used in the detection and regular

follow-up of UC instead of using painful and costly cystoscopy. In addition, with the promising sensitivity and specificity for high-grade UC found in our samples, Raman microspectroscopy could be especially helpful in the early detection or verification of high-grade upper tract UC.

CONCLUSIONS

Raman spectral imaging, SHG, CARS, HCA, and a random forest classifier were used for the label-free identification of urothelial cells in urine sediments. Differentiation between normal and high-grade cancerous urothelial cells was achieved automatically based on their Raman spectra with 100% accuracy using leave-one-patient-out cross-validation. A Raman marker band near 482 cm^{-1} , which originates from glycogen, can be used to differentiate normal and high-grade cancerous urothelial cells. The level of glycogen is lower in urothelial cancerous cells compared to normal urothelial cells, whereas the level of fatty and nucleic acids is increased upon the progression of urothelial carcinoma. Thus, the vibrational fingerprint provided by the Raman spectra is now assigned in a clear-cut manner to metabolic changes within the cancer cells. Furthermore, this study shows the potential of Raman microspectroscopy as a noninvasive method for the diagnosis of high-grade UC in urine with high accuracy based on metabolic changes in urothelial cells. We also demonstrate that CARS/SHG microscopy has a prospective use as a fast label-free imaging tool for prescreening large amounts of cells in cytopathological samples. In the future, we aim to identify low-grade urothelial cancerous cells in the urine of patients not only using Raman spectra but also using cell morphology from CARS/SHG imaging.

ASSOCIATED CONTENT

Supporting Information

The Supporting Information is available free of charge on the ACS Publications website at DOI: 10.1021/acs.analchem.7b01403.

Preparation of urine samples for spectroscopic measurements; classification of urothelial cells; workflow for the sample collection and preparation; SHG and CARS images of a large area of urine sediment; Raman mean spectra of the nucleus and cytoplasm of normal and high-grade cancerous cells; Raman spectrum of erythrocytes in urine sediment; and HE-stained images of normal and high-grade cancerous urothelial cells (PDF)

AUTHOR INFORMATION

Corresponding Author

*E-mail: gerwert@bph.rub.de. Phone: +49-234-32-24461.

ORCID

Samir F. El-Mashtoly: 0000-0001-6087-8817

Notes

The authors declare no competing financial interest.

ACKNOWLEDGMENTS

We thank Dr. Sven Bruker for useful discussions. This research was supported by the Protein Research Unit Ruhr within Europe (PURE), Ministry of Innovation, Science and Research (MIWF) of North-Rhine Westphalia, Germany, and the European Regional Development Fund, European Union and North-Rhine Westphalia, Germany.

REFERENCES

- (1) Ferlay, J.; Soerjomataram, I.; Dikshit, R.; Eser, S.; Mathers, C.; Rebelo, M.; Parkin, D. M.; Forman, D.; Bray, F. *Int. J. Cancer* **2015**, *136*, E359–386.
- (2) Jemal, A.; Bray, F.; Center, M. M.; Ferlay, J.; Ward, E.; Forman, D. *Ca-Cancer J. Clin.* **2011**, *61*, 69–90.
- (3) Babjuk, M.; Burger, M.; Zigeuner, R.; Shariat, S. F.; van Rhijn, B. W. G.; Compérat, E.; Sylvester, R. J.; Kaasinen, E.; Böhle, A.; Palou Redorta, J.; Rouprêt, M. *Eur. Urol.* **2013**, *64*, 639–653.
- (4) Lotan, Y.; Kamat, A. M.; Porter, M. P.; Robinson, V. L.; Shore, N.; Jewett, M.; Schelhammer, P. F.; White, R.; Quale, D.; Lee, C. T. *Cancer* **2009**, *115*, 4096–4103.
- (5) Koss, L. G.; Deitch, D.; Ramanathan, R.; Sherman, A. B. *Acta Cytol.* **1985**, *29*, 810–816.
- (6) Lotan, Y.; Roehrborn, C. G. *Urology* **2003**, *61*, 109–118.
- (7) Krafft, C.; Schmitt, M.; Schie, I. W.; Cialla-May, D.; Matthäus, C.; Bocklitz, T.; Popp, J. *Angew. Chem., Int. Ed.* **2017**, *56*, 4392–4430.
- (8) Kong, K.; Kendall, C.; Stone, N.; Notingher, I. *Adv. Drug Delivery Rev.* **2015**, *89*, 121–134.
- (9) Kong, K.; Rowlands, C. J.; Varma, S.; Perkins, W.; Leach, I. H.; Koloydenko, A. A.; Williams, H. C.; Notingher, I. *Proc. Natl. Acad. Sci. U. S. A.* **2013**, *110*, 15189–15194.
- (10) Byrne, H. J.; Baranska, M.; Puppels, G. J.; Stone, N.; Wood, B.; Gough, K. M.; Lasch, P.; Heraud, P.; Sulé-Suso, J.; Sockalingum, G. D. *Analyst* **2015**, *140*, 2066–2073.
- (11) Blackledge, J.; Dubovitskiy, D. Targeting cell nuclei for the automation of raman spectroscopy in cytology. Patent WO2014053520 (A1), 2014.
- (12) Krause, M.; Rösch, P.; Radt, B.; Popp, J. *Anal. Chem.* **2008**, *80*, 8568–8575.
- (13) Kong, K.; Zaabar, F.; Rakha, E.; Ellis, I.; Koloydenko, A.; Notingher, I. *Phys. Med. Biol.* **2014**, *59*, 6141–6152.
- (14) Kerr, L. T.; Domijan, K.; Cullen, I.; Hennelly, B. M. *Photonics Lasers Med.* **2014**, *3*, 193 DOI: 10.1515/plm-2014-0004.
- (15) Stone, N.; Kendall, C.; Smith, J.; Crow, P.; Barr, H. *Faraday Discuss.* **2004**, *126*, 141.
- (16) Barman, I.; Dingari, N. C.; Singh, G. P.; Kumar, R.; Lang, S.; Nabi, G. *Anal. Bioanal. Chem.* **2012**, *404*, 3091–3099.
- (17) Draga, R. O. P.; Grimbergen, M. C. M.; Vijverberg, P. L. M.; van Swol, C. F. P.; Jonges, T. G. N.; Kummer, J. A.; Ruud Bosch, J. L. H. *Anal. Chem.* **2010**, *82*, 5993–5999.
- (18) Crow, P.; Molckovsky, A.; Stone, N.; Uff, J.; Wilson, B.; WongKeeSong, L.-M. *Urology* **2005**, *65*, 1126–1130.
- (19) Grimbergen, M. C. M.; van Swol, C. F. P.; Draga, R. O. P.; van Diest, P.; Verdaasdonk, R. M.; Stone, N.; Bosch, J. H. L. R. *SPIE BiOS: Biomedical Optics* **2009**, 716114.
- (20) Crow, P.; Uff, J. S.; Farmer, J. A.; Wright, M. P.; Stone, N. *BJU Int.* **2004**, *93*, 1232–1236.
- (21) de Jong, B. W. D.; Bakker Schut, T. C.; Maquelin, K.; van der Kwast, T.; Bangma, C. H.; Kok, D.-J.; Puppels, G. J. *Anal. Chem.* **2006**, *78*, 7761–7769.
- (22) Stone, N.; Kendall, C.; Shepherd, N.; Crow, P.; Barr, H. J. *J. Raman Spectrosc.* **2002**, *33*, 564–573.
- (23) Canetta, E.; Mazilu, M.; De Luca, A. C.; Carruthers, A. E.; Dholakia, K.; Neilson, S.; Sargeant, H.; Briscoe, T.; Herrington, C. S.; Riches, A. C. J. *J. Biomed. Opt.* **2011**, *16*, 037002.
- (24) Praveen, B. B.; Mazilu, M.; Marchington, R. F.; Herrington, C. S.; Riches, A.; Dholakia, K. *PLoS One* **2013**, *8*, e67211.
- (25) Harvey, T. J.; Hughes, C.; Ward, A. D.; Faria, E. C.; Henderson, A.; Clarke, N. W.; Brown, M. D.; Snook, R. D.; Gardner, P. J. *J. Biophotonics* **2009**, *2*, 47–69.
- (26) Shapiro, A.; Gofrit, O. N.; Pizov, G.; Cohen, J. K.; Maier, J. *Eur. Urol.* **2011**, *59*, 106–112.
- (27) El-Mashtoly, S. F.; Niedieker, D.; Petersen, D.; Krauss, S. D.; Freier, E.; Maghnouj, A.; Mosig, A.; Hahn, S.; Kötting, C.; Gerwert, K. *Biophys. J.* **2014**, *106*, 1910–1920.
- (28) El-Mashtoly, S. F.; Petersen, D.; Yosef, H. K.; Mosig, A.; Reinacher-Schick, A.; Kötting, C.; Gerwert, K. *Analyst* **2014**, *139*, 1155–1161.
- (29) El-Mashtoly, S. F.; Yosef, H. K.; Petersen, D.; Mavarani, L.; Maghnouj, A.; Hahn, S.; Kötting, C.; Gerwert, K. *Anal. Chem.* **2015**, *87*, 7297–7304.
- (30) Yosef, H. K.; Mavarani, L.; Maghnouj, A.; Hahn, S.; El-Mashtoly, S. F.; Gerwert, K. *Anal. Bioanal. Chem.* **2015**, *407*, 8321–8331.
- (31) Krauß, S. D.; Petersen, D.; Niedieker, D.; Fricke, I.; Freier, E.; El-Mashtoly, S. F.; Gerwert, K.; Mosig, A. *Analyst* **2015**, *140*, 2360–2368.
- (32) Rathert, P.; Roth, S. *Urinzytologie: Praxis und Atlas*, 1995.
- (33) Diem, M. *Modern Vibrational Spectroscopy and Micro-Spectroscopy: Theory, Instrumentation, And Biomedical Applications*; John Wiley & Sons, Inc: Chichester, West Sussex, 2015.
- (34) Campagnola, P. J.; Dong, C.-Y. *Laser Photonics Rev.* **2011**, *5*, 13–26.
- (35) de Lanerolle, P.; Serebryanny, L. *Nat. Cell Biol.* **2011**, *13*, 1282–1288.
- (36) Chung, C.-Y.; Potma, E. O. *Annu. Rev. Phys. Chem.* **2013**, *64*, 77–99.
- (37) Krafft, C.; Schmitt, M.; Schie, I.; Cialla-May, D.; Matthäus, C.; Bocklitz, T.; Popp, J. *Angew. Chem., Int. Ed.* **2017**, *56*, 4392–4430.
- (38) Salzer, R.; Siesler, H. W. *Infrared and Raman Spectroscopic Imaging*; Wiley-VCH: Weinheim, 2009.
- (39) Rygula, A.; Majzner, K.; Marzec, K. M.; Kaczor, A.; Pilarczyk, M.; Baranska, M. J. *J. Raman Spectrosc.* **2013**, *44*, 1061–1076.
- (40) Konorov, S. O.; Schulze, H. G.; Atkins, C. G.; Piret, J. M.; Aparicio, S. A.; Turner, R. F. B.; Blades, M. W. *Anal. Chem.* **2011**, *83*, 6254–6258.
- (41) Mavarani, L.; Petersen, D.; El-Mashtoly, S. F.; Mosig, A.; Tannapfel, A.; Kötting, C.; Gerwert, K. *Analyst* **2013**, *138*, 4035–4039.
- (42) Nielsen, M.; Qaseem, A. *Ann. Intern. Med.* **2016**, *164*, 488.
- (43) Davis, R.; Jones, J. S.; Barocas, D. A.; Castle, E. P.; Lang, E. K.; Leveille, R. J.; Messing, E. M.; Miller, S. D.; Peterson, A. C.; Turk, T. M. T.; Weitzel, W. J. *Urol.* **2012**, *188*, 2473–2481.
- (44) Terashima, M.; Fujita, Y.; Togashi, Y.; Sakai, K.; De Velasco, M. A.; Tomida, S.; Nishio, K. *Oncotarget* **2014**, *5*, 7040–7050.
- (45) Lew, C. R.; Guin, S.; Theodorescu, D. *Nat. Rev. Urol.* **2015**, *12*, 383–391.
- (46) Vander Heiden, M. G.; Cantley, L. C.; Thompson, C. B. *Science* **2009**, *324*, 1029–1033.
- (47) Breiman, L. *Mach. Learn.* **2001**, *45*, 5–32.
- (48) Hajdinjak, T. *Urol. Oncol.* **2008**, *26*, 646–651.
- (49) Giannopoulos, A.; Manousakas, T.; Gounari, A.; Constantinides, C.; Choremi-Papadopoulou, H.; Dimopoulos, C. J. *Urol.* **2001**, *166*, 470–475.
- (50) van Rhijn, B. W. G.; van der Poel, H. G.; van der Kwast, T. H. *Eur. Urol.* **2005**, *47*, 736–748.
- (51) Pesch, B.; Taeger, D.; Johnen, G.; Gawrych, K.; Bonberg, N.; Schwentner, C.; Wellhäusser, H.; Kluckert, M.; Leng, G.; Nasterlack, M.; Lotan, Y.; Stenzl, A.; Brüning, T. *Int. Arch. Occup. Environ. Health* **2014**, *87*, 715–724.
- (52) Bonberg, N.; Taeger, D.; Gawrych, K.; Johnen, G.; Banek, S.; Schwentner, C.; Sievert, K.-D.; Wellhäusser, H.; Kluckert, M.; Leng, G.; Nasterlack, M.; Stenzl, A.; Behrens, T.; Brüning, T.; Pesch, B. *BJU Int.* **2013**, *112*, E372–E382.
- (53) Huber, S.; Schwentner, C.; Taeger, D.; Pesch, B.; Nasterlack, M.; Leng, G.; Mayer, T.; Gawrych, K.; Bonberg, N.; Pelster, M.; Johnen, G.; Bontrup, H.; Wellhäusser, H.; Bierfreund, H.-G.; Wiens, C.; Bayer, C.; Eberle, F.; Scheuermann, B.; Kluckert, M.; Feil, G.; Brüning, T.; Stenzl, A. *BJU Int.* **2012**, *110*, 699–708.